Scatter and Attenuation Correction for Brain SPECT Using Attenuation Distributions Inferred from a Head Atlas

Robert Z. Stodilka, Brad J. Kemp, Frank S. Prato, Andrew Kertesz, Don Kuhl, and Richard L. Nicholson

Department of Nuclear Medicine and Magnetic Resonance, and Department of Neurology, St. Joseph's Health Center; Lawson Research Institute, London; Department of Nuclear Medicine, London Health Sciences Center (Victoria Campus), London; and Department of Medical Biophysics, University of Western Ontario, London, Ontario, Canada

Sequential transmission scanning (TS)/SPECT is impractical for neurologically impaired patients who are unable to keep their heads motionless for the extended duration of the combined scans. To provide an alternative to TS, we have developed a method of inferring-attenuation distributions (IADs), from SPECT data, using a head atlas and a registration program. The validity of replacing TS with IAD was tested in 10 patients with mild dementia. **Methods:** TS was conducted with each patient using a collimated ^{99m}Tc line source and fanbeam collimator; this was followed by hexamethyl propyleneamine oxime–SPECT. IAD was derived by deformably registering the brain component of a digital head atlas to a preliminary SPECT reconstruction and then applying the resulting spatial transformation to the full head atlas. SPECT data were reconstructed with scatter and attenuation correction. Relative regional cerebral blood flow was quantified in 12 threshold-guided anatomic regions of interest, with cerebellar normalization. SPECT reconstructions using IAD were compared with those using TS (which is the "gold standard") in terms of these regions of interest. **Results:** When we compared all regions of interest across the population, the correlation between IAD-guided and TS-guided SPECT scans was 0.92 ($P < 0.0001$), whereas the mean absolute difference between the scans was 7.5%. On average, IAD resulted in slight underestimation of relative regional cerebral blood flow; however, this underestimation was statistically significant for only the left frontal and left central sulcus regions ($P = 0.001$ and 0.002, respectively). Error analysis indicated that approximately 10.0% of the total error was caused by IAD scatter correction, 36.6% was caused by IAD attenuation correction, 27.0% was caused by discrepancies in region-of-interest demarcation from quantitative errors in IAD-guided reconstructions, and 26.5% was caused by patient motion throughout the imaging procedure. **Conclusion:** SPECT reconstructions guided by IAD are sufficiently accurate to identify regional cerebral blood flow deficits of 10%, which are typical in moderate and advanced dementia.

Key Words: transmission imaging; brain SPECT

J Nucl Med 2000; 41:1569–1578

Efforts to establish an objective diagnosis of dementia using SPECT measurements of regional cerebral blood flow (rCBF) have had mixed success. For example, although some studies present evidence that rCBF deficits can be used as an index of severity in dementia (*1*) or to establish differential diagnoses among dementias, other studies cite SPECT measurements as being of limited value to objective diagnosis (*2*).

Confounds to the objective diagnosis of brain disease by SPECT originate from multiple sources: physical processes such as photon scatter and attenuation, the difficulties of using rCBF measurements to diagnose disease, the variability of radiopharmaceutical uptake (*3*), and subjective tasks performed on images such as region-of-interest (ROI) demarcation (*4*). Ideally, ROI placement should correspond to anatomically relevant features. Achieving this using functional data is problematic because of the low spatial resolution of emission tomography (*5,6*) and the potential discordance between functional and anatomic data (*5,7*). Objective diagnosis ultimately depends on establishing a correlation that can predict disease severity using rCBF, which can be difficult because of the lack of consensus regarding both ROI placement (*4*) and discriminative mathematic models (*1*).

Recent work has demonstrated the benefits that both scatter and attenuation correction offer to brain SPECT (*8,9*). For example, the use of these corrections allows the cortical concentration of ^{99m}Tc to be quantified, in a relative sense, with an error of approximately 5%. Without scatter correction, errors invariably increase to 10% or more. The inconsistent implementation of attenuation correction and sporadic use of scatter correction explain, at least in part, why the value of quantitative brain SPECT has not been established. The corrections that have been most successful in achieving this accuracy are based on physical models of photon propagation through nonuniform media. These models, in turn, have 2 dependencies: their general theoretic descriptions and how these descriptions are customized for each imaging situation. Popular combinations of theoretic descriptions include spatial scatter corrections (*8,10*) and

unified attenuation correction–reconstructions, such as maximum-likelihood expectation maximization (11). The application of these methods to individual SPECT scans requires estimates of tissue density distribution–attenuation maps. An increasingly emphasized method of providing such estimates is by transmission imaging (12,13).

Gamma-camera transmission imaging in the head is known to provide estimates of sufficient accuracy to fully exploit the current generation of theoretic descriptions of photon propagation (8,9). This is best exemplified by use of segmented transmission maps (14) for scatter and attenuation correction. Certainly, the information offered by transmission scanning will be better used by improved theoretic descriptions. However, transmission imaging is achieved at significant costs: increased imaging time, increased hardware complexity, and increased financial cost.

The subject of providing these estimates of tissue density— without increasing scan time—has recently received renewed attention; attempts to provide attenuation maps that are based on fast transmission scans, simultaneous emission–transmission scans (12,15), or exploiting the consistency conditions of the attenuated radon transform (16) are all examples. The fast and simultaneous transmission scan methods were developed to minimize both scan time and the artifacts associated with errors in scatter and attenuation correction caused by misaligned emission and transmission data (17). However, transmission imaging still suffers the penalty of requiring extra hardware. Panin et al. (18) have developed a method to extrapolate complete attenuation maps from truncated transmission scans. The method of Natterer (16) is an example of an attractive alternative: the estimation of attenuation maps from emission data alone, termed "inferring anatomy." Earlier attempts to infer anatomy included fitting ellipses to photopeak- or Compton-window sinograms or thresholding preliminary reconstructions (19). The success of applying these techniques to brain imaging would rest on the assumptions that (a) the attenuation properties of extracerebral tissue were negligible compared with the attenuation caused by the brain and (b) that the spatial distribution of the brain could be inferred from the SPECT data. Furthermore, these methods are known to require high uptake in superficial tissue and adequate counting statistics (17). Unfortunately, facial uptake of radiopharmaceuticals varies between individuals and the radiopharmaceuticals themselves (20), making these techniques sensitive to threshold selection (19). This is particularly true in the cerebellar regions, where differences between the brain and head contours are most pronounced (21,22). The use of Natterer's consistency conditions to infer anatomy may circumvent this confound. However, these conditions have been developed under the requirement of rejecting the 30% of photopeak counts that constitute scatter in brain imaging using ^{99m}Tc-based radiopharmaceuticals (8).

We have developed a method of inferring nonuniform attenuation distributions for the head from emission data by combining concepts from stereotactic surgery, intersubject multimodality registration, and anatomic atlases. Our method requires a digitized head atlas and a registration program. It is simple to implement, because no customized software is required, and is computationally feasible on modern desktop computers, requiring only slightly more computation time than a typical tomographic reconstruction. Furthermore, our method facilitates the retrospective application of modern nonuniform scatter and attenuation correction to preexisting brain SPECT databases. We expect this to improve the accuracy of posthoc quantitative statistical analyses, provide increased longitudinal and interinstitution standardization, and aid in the design of a normal brain SPECT database (23). The inference algorithm was previously validated with a tissue-equivalent anthropomorphic head phantom (24). In this article, we demonstrate its application to 10 ^{99m}Tc-hexamethyl propyleneamine oxime (HMPAO)– brain SPECT scans. Inferred anatomy is compared with transmission imaging in terms of template-based rCBF quantification (25) after nonuniform scatter and attenuation correction.

MATERIALS AND METHODS

Inferring Anatomy from a Head Atlas

Intersubject registration purports that there exists a transformation that maps analogous features from 2 different scans into the same spatial coordinates. We assumed that if such a transformation can be derived from 2 SPECT scans, the same transformation would register the 2 corresponding transmission scans. In this application, registration parameters were derived that transformed a SPECT head atlas into the same orientation as a patient SPECT scan.

A head atlas was prepared as follows. The Zubal 3-dimensional digitized MRI head phantom (26) was segmented to produce 2 datasets: a SPECT atlas, simulating a SPECT scan of the phantom, and an anatomic atlas, simulating a transmission scan of the phantom. The SPECT atlas consisted of voxels containing gray and white matter, to which ^{99m}Tc-HMPAO relative uptakes of 4 and 1 had been assigned, respectively. The anatomic atlas consisted of voxels containing hard and soft tissues and nasal sinuses, to which the respective 140-keV narrow-beam attenuation coefficients of 0.25, 0.15, and 0.075/cm had been assigned. The size of the atlas was modified to be consistent with the patient scans (described below): the atlas consisted of a 128 × 128 × 128 array of cubic voxels, in which each voxel had a side length of 3.2 mm.

A patient SPECT scan was then reconstructed—without scatter and attenuation correction—and facial activity was removed; this dataset is referred to as the preliminary patient reconstruction. The SPECT atlas then was registered to the preliminary reconstruction, and the spatial transformation was recorded. This transformation was then applied to the anatomic atlas, thus inferring the location of the patient's soft and hard tissues and air cavities (Fig. 1).

A general purpose radiologic analysis program (Hermes; Nuclear Diagnostics, Stockholm, Sweden) was used to perform the unimodality registration. The large variation in head orientation necessitated that a manual registration be performed first. This was followed by an automated refinement. The cost function of the automated registration was defined as the sum of absolute count
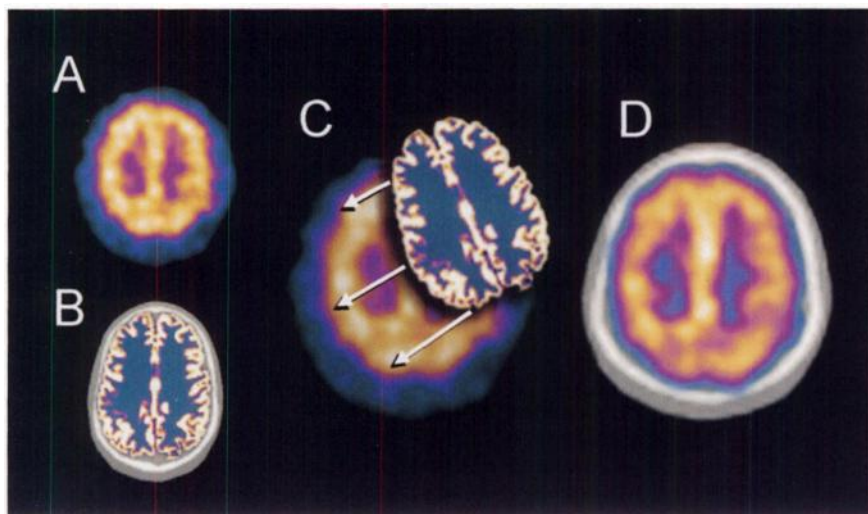
FIGURE 1. Inferred-anatomy algorithm requires patient's preliminary reconstruction (A) and head atlas (B). Preliminary reconstruction does not include scatter and attenuation correction. Head atlas consists of functional component (color) and anatomic component (gray scale). Functional component is then spatially registered to preliminary reconstruction (C), and this optimal transformation is recorded. Patient's anatomy is then inferred by applying same transformation to anatomic component of head atlas (D). Extracerebral uptake has been windowed out to enhance clarity of transmission scan.

differences (27). A global minimum was sought by a simplex search within a parameter space consisting of rotating, shifting, and linear scaling in x, y, and z directions (6).

Sequential Transmission and Emission Imaging

Ten patients with dementia (5 women, 5 men; mean age, 64.3 y) were analyzed. For each patient, a transmission scan was acquired. Patients relaxed during the quiet transmission scan and were then injected with 740 MBq ^{99m}Tc-HMPAO. The SPECT procedure was started approximately 5 min postinjection. The SPECT system, which has transmission capabilities, has been previously described in detail (13). It consists of a General Electric (Milwaukee, WI) 400AC/T gamma camera with a 409.6-mm diameter circular field of view. Projections were acquired through a fanbeam collimator (Nuclear Fields, Des Plaines, IL) that had a 600-mm focal length and a 1.5-mm flat-to-flat hexagon hole width. The transmission component consisted of a frame mounted onto the camera's collimator that held a tantalum-collimated ^{99m}Tc line source along the focal line of the fanbeam collimator. Collimation of both the line source and camera minimizes scatter; hence, the transmission system effectively measures narrow-beam attenuation coefficients (13). SPECT and transmission scans were acquired with a 20% energy window, centered on the ^{99m}Tc photopeak of 140 keV. The scans consisted of 128 projections, equally spaced over 360°. Each circular projection was acquired into a 128 × 128 pixel square matrix (1 pixel = 3.2 mm). Both transmission and SPECT scans were 10 s per projection; counting rates were approximately 40,000 and 1,500 counts/s, respectively. Total counts in transmission and SPECT scans were approximately 50 million and 2 million, respectively. All scans were corrected for uniformity using 100 million flood images, and transmission scans were normalized to 50 million blank images. Radii of rotation varied among the patients, with the smallest being 170 mm and the largest being 205 mm. Before reconstruction, all scans were rebinned to object-plane parallel-hole geometry by 2-dimensional cubic interpolation.

Scatter and Attenuation Correction and Reconstruction

The SPECT data were reconstructed using a maximum-likelihood estimator with an unregularized 32-level, ordered-subset (28) implementation of the expectation maximization (OSEM) algorithm (11). The 4 projections that were used per subiteration were equally spaced about 360°. Attenuation was modeled in the matched projector–back-projector pair, and a scatter estimate (8)

was added as an a priori background after forward projection (11). Both scatter and attenuation modeling incorporated the narrow-beam attenuation coefficients from transmission imaging or inferred anatomy. Detector response was not included. Four iterations of OSEM were used, after initialization with a uniform support that was derived from transmission reconstruction or inferred anatomy. Reconstructions were then postfiltered by a 3-dimensional Butterworth filter with an order of 8 and magnitude of 0.42/cm. The transmission data were also reconstructed by the emission OSEM algorithm, after blank scan normalization and log transformation.

Line-source collimation, coupled with limitations in detector counting-rate capability and patient compliance, resulted in poor transmission statistics. To reduce the effects of transmission-imaging noise propagation into the SPECT reconstruction, the transmission reconstructions were segmented as follows. Soft tissue in the reconstructed transmission volumes was forced to have uniform density: first, a large ROI was drawn around soft-tissue regions, and mean and variance estimates were calculated. Then, all voxels having count densities within ±2 SDs of this mean were assigned to an attenuation coefficient 0.15/cm. Thus, the transmission reconstructions were characterized by noiseless soft tissue, yet featured hard tissue and air cavities.

Template-Based Quantification

Previous work has shown that a major confound to reproducible quantification originates from manual and threshold-dependent placement of anatomic ROIs onto SPECT scans (25). To eliminate this subjective source of error, we previously developed a normal template (25) onto which 12 bilateral volumetric ROIs have been demarcated (1). The ability to store the template and its ROIs ensures reproducibility of the analysis. This quantification procedure also introduces standardization to the analysis, which facilitates the exchange of data among different institutions (5). All reconstructed scans were registered to the normal template; this registration is referred to as spatial normalization. Before spatial normalization, voxels previously identified as facial activity were set to zero. ROIs were placed onto 17 adjacent slices in the cerebral cortex and 4 adjacent slices in the cerebellum. After superposition of the template ROIs onto each scan, the cortical rCBF for each ROI was normalized to cerebellar rCBF (1) and corrected for blood

flow–dependent tracer reflux (29). The cerebellar normalization constant is taken to be the average of left and right cerebellar rCBF. Analysis of the absolute concentration of the radiopharmaceutical was not performed; currently, absolute rCBF quantification is seldom used in SPECT.

Quantitative Error Analysis

For visual comparison, a sample of inferred-anatomy and transmission reconstructions is shown in Figure 2. In Figure 3, we show profiles through the SPECT reconstructions that were guided by transmission scans and inferred anatomy. The profiles have not been normalized to cerebellar count density.

The means and standard errors of rCBF from SPECT scans that were guided by inferred-anatomy and transmission scans were compared ROI by ROI (Fig. 4). Statistical analysis was also performed ROI by ROI using repeated ANOVA to determine where there were significant differences between the inferred-anatomy versus transmission-guided reconstruction methods. Pooled-ROI and ROI-dependent correlation coefficients were calculated between inferred-anatomy and transmission-guided SPECT reconstructions. Figure 5 shows the correlation between the 2 reconstruction and quantification methods by pooling all ROIs and patients. The P value was 0.05 for all tests.

Error Propagation Analysis

Four sources of error were found that contributed to the above discrepancies in ROI quantification: inferred-anatomy–guided scatter correction; inferred-anatomy–guided attenuation correction; inferred-anatomy–guided spatial normalization, which is equivalent to ROI misplacement; and patient motion between transmission and SPECT scans. The first 2 sources are inherent limitations to the principle of inferred anatomy, whereas the last 2 represent artifact exaggerations of errors in the context of this study. The first 3 sources of error—scatter, attenuation, and ROI misplacement—were measured.

The propagation of ROI quantification to differences between inferred-anatomy– and transmission-guided scatter correction were analyzed by performing inferred-anatomy–derived scatter correction, performing transmission-derived attenuation correction, and applying the spatial normalization calculated to be optimal for registering the transmission-derived SPECT reconstruction to the quantification template. A similar analysis followed for evaluating the effects of inferred-anatomy–derived attenuation correction: transmission-derived scatter correction, inferred-anatomy–derived attenuation correction, and application of the spatial normalization that was calculated to be optimal for registering the transmission-derived SPECT reconstruction to the quantification template. The effects of ROI misplacement were quantified by performing transmission-derived scatter and attenuation correction but then applying the spatial transformation calculated to be optimal for registering the inferred-anatomy–derived SPECT reconstruction to the quantification template. Thus, the full propagation analysis resulted in 3 reconstructions (each of which was quantitatively compared by the above-described, template-based quantification procedure) with the "gold-standard," transmission-derived SPECT reconstruction and spatial normalization. This procedure was performed for the 10 patients, and the results were averaged. However, once the errors from scatter, attenuation, and ROI misplacement were separately quantified, their totals were found to be less than the errors caused by the full inferred-anatomy protocol. This additional source of error is termed "unaccountable" and is believed to be caused by patient motion.

RESULTS

Qualitative Analysis

A sample comparison of inferred-anatomy and transmission reconstructions is shown in Figure 2 for midsagittal and cortical–axial slices. There was accurate reproduction of soft and hard tissues at the cortical level, as shown in the figure. Some discrepancy can be seen near the vertex; however, this region is seldom included in quantitative analysis. Discrepancies near the nasal sinus are most marked. It is unlikely
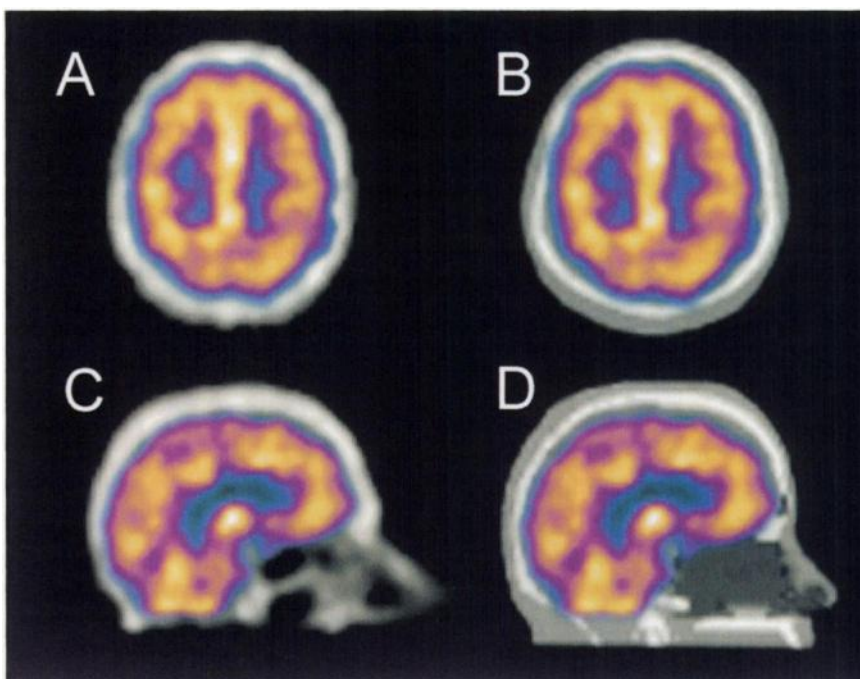

FIGURE 2. Examples of patient's SPECT scan (color) superimposed onto pertinent transmission reconstruction (A and C; gray scale) and inferred anatomy (B and D; gray scale). SPECT reconstruction includes scatter and attenuation correction guided by either transmission reconstruction or inferred anatomy. Visually, inferred anatomy was found to reproduce tissue distribution in cortical areas well but had difficulties at cerebellar level where nasal cavities were found to be very patient specific. Extracerebral uptake has been windowed out to enhance clarity of transmission scan.
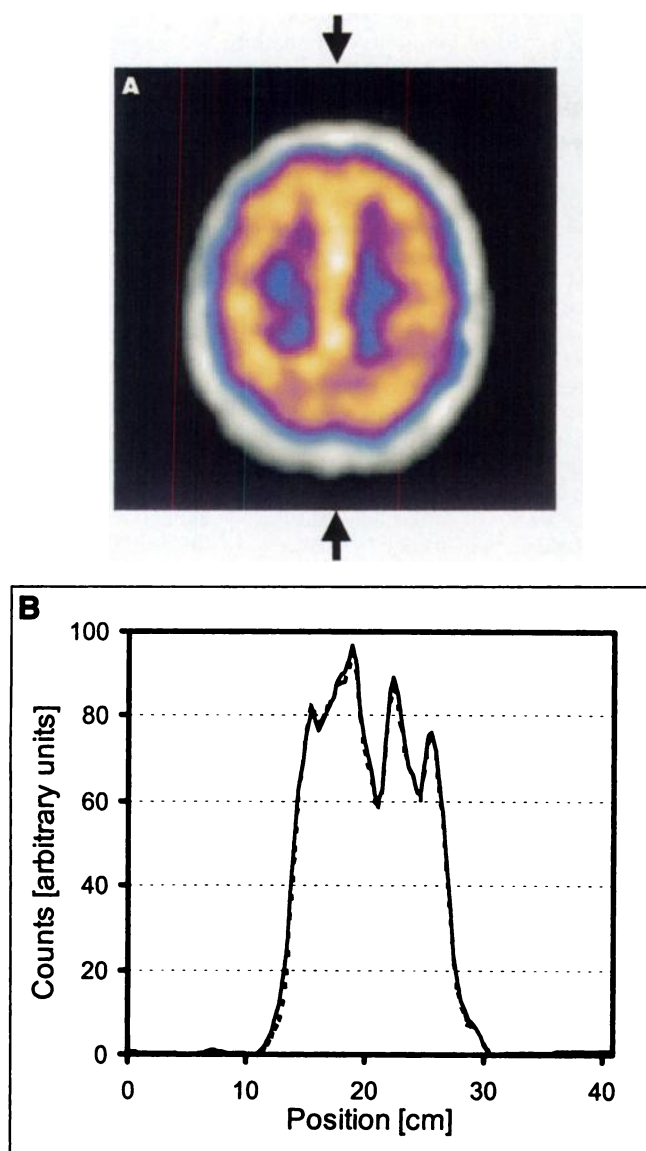
FIGURE 3. Reconstructions at cortical–axial level (A) and respective profiles (B) comparing SPECT reconstruction guided by pertinent transmission scan (solid line) with reconstruction guided by inferred anatomy (dashed line). Profiles were taken between the 2 arrows in A.

FIGURE 4. rCBF with voxel-by-voxel Lassen's correction, relative to cerebellum is shown for 12 bilateral ROIs. Means and standard errors are calculated across 10 patients. Quantification follows scatter and attenuation correction guided by transmission reconstructions (O) or inferred anatomy (□). On average, reconstructions guided by inferred anatomy tended to underestimate relative rCBF; this underestimation is statistically significant for left frontal and left central sulcus ROIs. Bars represent SEM.

imaging with the same SPECT reconstruction guided by inferred anatomy. The profile was taken along the longest axis of the head, which is most sensitive to misregistered transmission maps after scatter and attenuation correction (*30*).

that these differences can be reconciled with our registration procedure.

Many SPECT scans were found to contain significant extracerebral activity, such as facial activity (not shown). Unfortunately, limited patient compliance and our sequential transmission-emission protocol did not afford us the option of delayed SPECT imaging after radiopharmaceutical administration—an option that is known to reduce such nonspecific uptake. (Scatter correction was observed to substantially reduce extracerebral reconstructed activity [not shown], which may have implications for registration accuracy [see Discussion].)

Using midbrain profiles, as shown in Figure 3, we compared a SPECT reconstruction guided by transmission
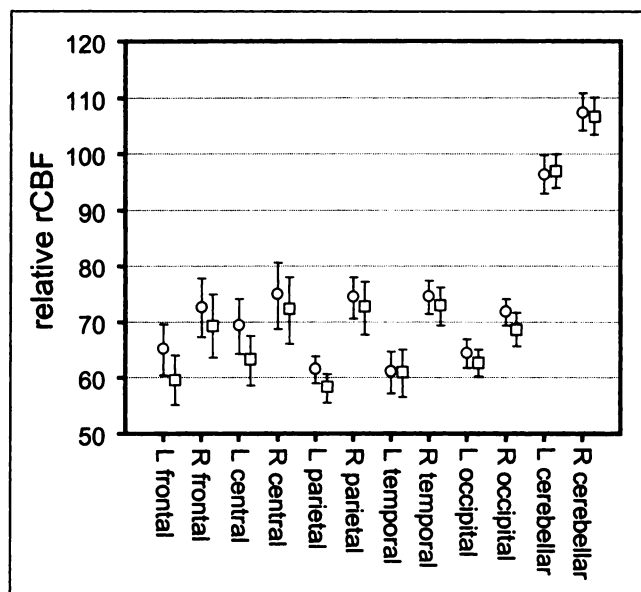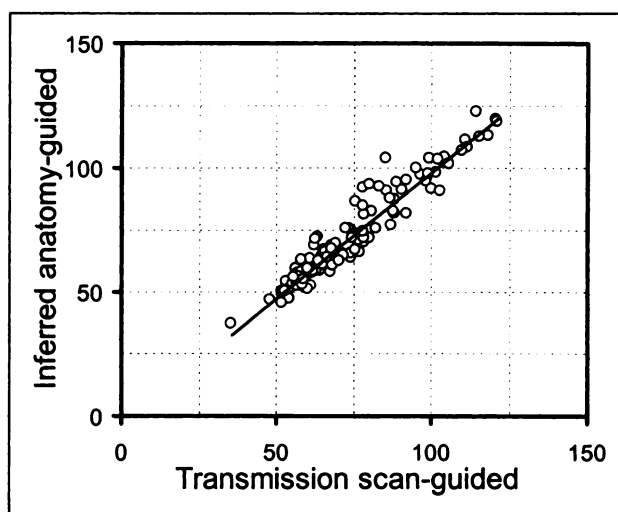

FIGURE 5. Comparison of reconstructions guided by transmission scans (abscissa) with reconstructions guided by inferred anatomy (ordinate). One hundred and twenty data points are shown; these are from 12 ROIs and 10 patients. Each point represents rCBF with Lassen's correction, relative to cerebellum. Equation of line of best fit is $y = 1.02x - 3.83$, and $R^2 = 0.92$ ($P < 0.0001$).

Quantitative Error Analysis

Table 1 shows the results of the repeated ANOVA and correlation analysis in which we compared transmission reconstruction and inferred-anatomy–guided reconstruction and quantification. Left frontal and central sulcus ROIs showed the highest probability of a true difference, reaching statistical significance with $P = 0.001$ and 0.002, respectively. These ROIs also had the highest correlation coefficients relating transmission reconstruction– and inferred-anatomy–guided SPECT reconstruction and quantification. Interestingly, the left frontal and central sulcus ROIs were also found to have marked rCBF deficits, suggesting that inferred anatomy may have difficulties near regions with substantially reduced radiopharmaceutical uptake.

Figure 4 shows the means and standard errors for transmission reconstruction and inferred anatomy in each of the 12 ROIs, averaged across the entire population. The mean absolute difference for all ROIs across the whole population was 7.5%. Correlation for all ROIs and all patients was found to be high ($R = 0.92$; Fig. 5).

Error Propagation Analysis

The results from the propagation analysis are presented in Table 2. These results are presented as errors relative to the gold standard transmission-reconstruction–guided reconstruction and spatial normalization. We found that errors in scatter distribution estimates resulted in approximately 10.0% of the total quantitative error; attenuation correction, 36.6%; and ROI misplacement, 27.0%. The relative contributions of inferred-anatomy–derived scatter and attenuation correction to the total error seem credible: compensating for attenuation is of considerably greater consequence than removing

TABLE 2
Sources of Error from Inferring Anatomy, Averaged Across 10 Patients

Region	Scatter correction (%)	Attenuation correction (%)	ROI misplacement (%)	Unaccountable error (%)*
L frontal	6.1	44.5	28.6	20.8
R frontal	12.0	49.9	29.4	8.7
L central sulcus	5.7	40.4	17.9	36.0
R central sulcus	6.3	34.3	16.0	43.4
L parietal	7.9	25.7	30.3	36.1
R parietal	10.0	34.1	25.9	30.0
L temporal	10.0	38.3	20.0	31.8
R temporal	13.8	27.0	30.7	28.5
L occipital	13.2	23.2	27.6	36.0
R occipital	8.3	22.5	29.0	40.2
L cerebellar	13.5	48.7	31.9	5.8
R cerebellar	12.5	50.2	36.4	0.8
Average	10.0	36.6	27.0	26.5

*Right column indicates percentage of total differences that could not be accounted for by inferring anatomy. We believe that principal source of this error is patient motion.

Table summarizes percentage that each error source contributed to total quantitative differences between SPECT reconstructions guided by transmission scans or inferred anatomy.

TABLE 1
Repeated ANOVA Comparing rCBF Derived from SPECT Reconstructions Guided by Transmission Scans with Reconstructions Guided by Inferred Anatomy

Region	ANOVA significance	Paired sample correlation	Paired sample significance
L frontal	0.001*	0.965	<0.001
R frontal	0.088	0.953	<0.001
L central sulcus	0.002*	0.957	<0.001
R central sulcus	0.234	0.937	<0.001
L parietal	0.092	0.772	0.009
R parietal	0.473	0.862	0.001
L temporal	0.957	0.939	<0.001
R temporal	0.397	0.835	0.003
L occipital	0.271	0.835	0.003
R occipital	0.073	0.858	0.001
L cerebellar	0.545	0.938	<0.001
R cerebellar	0.603	0.925	<0.001

*Left frontal and left central sulcus regions showed highest probability of a true difference, with $P = 0.001$ and 0.002, respectively.

Right column indicates significance of paired sample correlation. Means and standard errors are presented graphically in Figure 4.

scattered photons. Furthermore, the effects of ROI misplacement, which were from errors in spatial normalization, were unexpectedly high; this confound is often overlooked in quantitative studies. Approximately 26.5% of the total discrepancy between inferred anatomy and transmission imaging could not be accounted for in the error propagation analysis of scatter, attenuation, and ROI misplacement. We hypothesize that this source of error is external to postacquisition data processing—the most likely source of error is patient motion during data acquisition. The effects of patient motion were not explicitly examined; the reader is referred to Andersson et al. (17) for a comprehensive analysis.

DISCUSSION

Currently, nonuniform scatter and attenuation correction depend on transmission imaging; this dependence represents a significant burden to emission tomography. The complexity and cost of hardware are increased, and acquiring a second dataset lengthens scan time. The potential value of inferred anatomy for brain SPECT is to provide a convenient, high-resolution, and noise-free substitute for transmission imaging. This benefit can be attained retroactively because inferred anatomy can be applied to any perfusion-type brain SPECT scan, for which nonuniform scatter and attenuation correction are sought, provided that the photopeak projections are available. Furthermore, although inferred anatomy has been validated for SPECT, its application can be potentially extended to PET imaging of the brain.

Quantitative rCBF errors caused by inferred anatomy are attributable to 4 sources: limitations in scatter and attenuation correction, misregistration of the atlas, ROI misplacement, and patient-specific discrepancies compared with the atlas that cannot be reconciled with any registration algorithm. We restrict discussion to the last 3; the reader is referred elsewhere for a detailed evaluation of the errors caused by scatter and attenuation correction (8).

Qualitative and Quantitative Comparisons

Comparing inferred-anatomy with transmission reconstructions indicated accurate reproduction of soft and hard tissues in cortical areas for all 10 patients. However, in many scans, clear discrepancy was indicated near the sinus cavity, as shown in Figure 2. Despite this shortcoming, we expected inferred anatomy to be more robust and accurate in providing estimates of underlying tissue distribution than fitting ellipses to photopeak emission data. The technique of fitting ellipses depends on adequate facial activity because the contours of the brain and head differ so considerably at the level of the cerebellum. Facial activity should not form the basis for estimating underlying tissue distributions because uptake varies with radiopharmaceutical and time between injection and scanning (20), making it an unreliable dependency. (The qualitative similarities demonstrated between inferred-anatomy and transmission reconstructions indicate confidence in accurately guiding scatter and attenuation correction; however, it is important to note that similar shape is a sufficient but not necessary prerequisite for accurate scatter and attenuation correction (16)).

Slight truncation effects were noticed on the transmission images for 3 of the 10 scans. Truncation occurred for kyphotic patients with broad shoulders or with short necks. This limitation was generally restricted to transaxial slices below the level of the cerebellum or very near its base, where the gamma camera's circular field of view proved to be inconvenient. The truncation only involved nasal cartilage and, therefore, was not expected to significantly impact results, as was demonstrated in the quantitative accuracy exhibited at the cerebellar level (Fig. 4).

Inferred anatomy had difficulties in regions with marked rCBF deficit, such as the left frontal lobe. Although frontal lobes generally exhibit high variability in HMPAO uptake (3), only the left frontal lobe had statistically significant error. This suggests that regional quantitative errors incurred by inferred anatomy are associated with rCBF deficits; however, previous studies have demonstrated that they may also be sensitive to spatial region. Achieving strong quantitative accuracy in extended sources is often difficult; this is particularly true with peripheral ROIs, where reconstructed activity is most sensitive to misregistration of the attenuating medium (30). For example, in the brain, a mismatch between emission and transmission data ≤ 5 mm can produce a 10% error in a 10-mm-thick peripheral cortical ROI (17,30). In general, extended sources, such as the brain, are affected by misregistration more than compact sources, such as the heart (17). Because the brain is elliptical, we expected that regions along the periphery of the long axis of the head would be more sensitive to attenuation-map misregistration than those along the short axis.

Choice of Head Atlas

Our method of inferring anatomy required a 2-component head atlas: a functional component that simulates a SPECT scan and an anatomic component that simulates a transmission scan. These components were derived from the head atlas of Zubal et al. (26), which is a 3-dimensional segmented MRI scan of a patient. Our use of the phantom of Zubal et al. agrees with a study by Andersson et al. (31), who demonstrated that simple segmentation of MRI data by thresholding would yield simulated PET images that were realistic enough to permit accurate intrapatient registration. Although the use of single-patient atlases, such as that that developed by Talairach et al. (32), have been successful as registration templates, there is an important conceptual limitation to their application. Features that are patient-specific anomalies, rather than general representations of the population, bias the success of applying single-patient atlases toward a narrow cross-section of the population with similar anomalies. Realizing this, some researchers have started generating atlases by amalgamating many scans (18,25), which are expected to be more applicable to the general population. However, the development of more specialized (i.e., disease, tracer, sex, age, or race specific) atlases should not be ruled out (31). For example, in this study, the gray-matter:white-matter activity ratio in the atlas of Zubal et al. was set at 4:1 (33), which is believed to be the gray-matter:white-matter ratio of rCBF in healthy tissue. An atlas with reduced contrast, however, may be more suitable: Podreka et al. (34), using SPECT, reported the observed gray-matter:white-matter ratio of HMPAO concentration to be approximately 2:1.

An example of a patient-specific anomaly is the nasal sinus of the Zubal et al. atlas (26). This sinus was found to be substantially larger than that of any patient in this study. In an earlier evaluation of inferred anatomy, conducted on a fully tissue equivalent anthropomorphic head phantom (Radiology Support Devices, Long Beach, CA), we found that the large sinus underestimated cerebellar count density by 10% (24). In this study, the large sinus cavity was obviously misrepresentative of the patient population. Therefore, we set its attenuation coefficient to 0.075/cm rather than manually reducing its size. In general, the sinus cavities were the most disparate structures among the patients, suggesting that subtle discrepancies will remain regardless of the selection of head atlas.

Attenuation distributions provided by inferred anatomy are of substantially higher resolution than typical transmission images. Although previous studies, particularly lung scans, have found that resolution mismatch between transmission and SPECT scans can lead to artifacts in the latter scan, these artifacts are restricted to being in close proximity to interfaces of heterogeneous density, such as between soft and hard tissues or tissue and air boundaries (35). These

artifacts should be minimal in this study because no ROIs crossed transmission-reconstruction or inferred-anatomy density interfaces.

Transmission reconstructions, before soft-tissue segmentation, were found to be very noisy. (Transmission projection counts at the cortical level, after blank scan normalization and log transformation, were characterized by a signal-to-noise ratio of approximately 5.) Previous theoretical (*36*) and experimental (*14*) work have demonstrated that this noise deleteriously propagates into the SPECT reconstruction. Attenuation correction that is based on segmented maps reduces this noise (*14*), and we have previously demonstrated a similar finding for scatter correction (*8*), although the effect is less dramatic because scatter estimates are generally smooth. Therefore, the reconstructed transmission scans were segmented as described in the Materials and Methods section.

Registration Procedure

Inferred anatomy relies on automated registration of an atlas to a patient scan. The accuracy of the registration procedure depends on the quality of both the registration algorithm and the data involved. Spatial registration of functional images does not imply concomitant anatomic registration (*7*). Although registration should be based on anatomic measurements, registration in radiopharmaceutical imaging is based on the assumption that the reconstructed distribution of radiopharmaceuticals is representative of the underlying anatomy. The validity of this assumption is unpredictable because of the inconsistencies between tissue distribution, true radiopharmaceutical distribution, and reconstructed radiopharmaceutical distribution; hence, the assumption has been the subject of some debate (*5,7*).

In this study, we found that the largest errors induced by inferred anatomy were within regions with significant deficits in rCBF. On average, inferring anatomy caused radiopharmaceutical concentration to be underestimated. This artifact was attributable to the underestimation of head size in regions that were proximal to rCBF deficits (*30*). Similar effects were noticed by Evans et al. (*5*), who found registration errors proximal to regions were the cortical ribbon had been inwardly displaced. Tsao et al. (*37*) found that local concavities in radiopharmaceutical uptake degraded registration. In the latter study, these concavities were caused by focal pathologic lesions, whereas for Evans et al., the apparent cortical displacement was an artifact of inadequate attenuation correction and resolution smearing.

Methods to minimize patient-specific misregistration fall into 2 categories: modifications to the data before registration and modifications to registration algorithms. Examples of the first method include filling local concavities of radiopharmaceutical uptake in an individual scan by transforming the image into a convex hull (*37*) or developing tracer- or lesion-specific atlases (*5,31*). The success of inferring anatomy from an atlas requires that the spatial relationship between the functional and anatomic data be the same for the patient and the atlas because this relationship

provides the basis for validly extrapolating the distribution of extracerebral tissue. However, the relationship is expected to break down with atrophy (brain shrinkage), because these changes are obviously not accompanied by similar head shrinkage. As implemented currently, inferred anatomy would underestimate the size of the head if the patient suffered from atrophy. Atrophy has already been demonstrated to be of concern in other aspects of quantitative brain studies (*38*). Furthermore, with regard to cardiac application, we expect inferred anatomy to encounter some difficulty because there is no fixed relationship between the size and shape of the heart and the surrounding attenuating medium: the lungs, chest, and breasts.

Automatic registration of 2 studies is based on the assumption that a cost function can be defined that reaches an optimum value when the 2 studies are perfectly registered. The topology of volumetric cost functions may be affected by many features, such as lesions and facial activity. We selected the sum of absolute differences, which has been previously used in brain imaging (*25,27*). However, this cost function, when used in conjunction with the simplex search (*27*), required operator intervention to define a set of starting orientation parameters (i.e., a good starting estimate) to minimize convergence to an undesirable local minimum. Holman et al. (*6*) found similar starting-parameter prerequisites to ensure accurate convergence of multimodality surface-matching registration.

Successful registration implies that, before registration, images have been corrected for scatter and attenuation (*39*) and resolution (*40*). These corrections would strengthen the relationship between the true and reconstructed distributions of radiopharmaceuticals. However, such corrections must be applied with caution because registration accuracy may be adversely affected if the emission images contain artifacts that are from misregistered attenuation maps. In this study, this correction would have confounded both registration of the head atlas to the preliminary reconstruction and, subsequently, spatial normalization to the quantification template. Consequently, we applied neither scatter nor attenuation correction to the preliminary reconstructions to minimize the first confound, whereas the second was treated in the error propagation analysis.

Higher spatial resolution of the SPECT scan would probably have reduced the errors associated with registering the atlas of Zubal et al. (*26*) to the preliminary SPECT reconstruction. Because scatter and attenuation correction are guided by this atlas, SPECT resolution limitations must contribute to errors in the corrections. However, misguided scatter and attenuation correction should not degrade spatial resolution. Consequently, we do not expect SPECT resolution limitations to contribute to the ROI misplacement error component.

Extracerebral activity is known to adversely affect registration accuracy (*31*). For example, deleting facial activity significantly improves the accuracy of automated registration (*25*). In this study, facial activity was manually deleted

from preliminary registrations before inferring anatomy and to final reconstructions before spatial normalization, because neither the head atlas nor quantification template contain facial activity. However, the reproducibility of subjective segmentation tasks is unknown; a similar concern led to the development of automated registration. Therefore, it would be valuable to have an objective method to minimize extracerebral activity. Also of concern, we noticed that scatter correction substantially reduced extracerebral activity. This is expected because reducing the scatter content of images has been shown to improve artifactually reduced contrast between regions of discordant radiopharmaceutical uptake (8,9). The deconvolution scatter kernel of Floyd et al. (10) is an ideal scatter model for this purpose because it does not depend on prior estimates of anatomy.

CONCLUSION

This study has introduced inferring anatomy from a head atlas for the purpose of applying nonuniform scatter and attenuation correction to brain SPECT without transmission scanning. Performance was evaluated by comparing SPECT reconstructions guided by inferred anatomy with SPECT reconstruction guided by transmission imaging. Data were obtained from a sample of patients with dementia. Three sources of errors were analyzed: scatter correction, attenuation correction, and ROI misplacement. Together, these errors accounted for approximately 73.6% of the total differences between SPECT reconstructions guided by inferred-anatomy and transmission scans; unaccountable errors were attributed to patient motion during the sequential transmission/SPECT protocol. Inferred anatomy has been shown to be successful in a clinical setting; future work should focus on improving quantitative accuracy by refining the head atlas, the registration algorithm, and the automated removal of extracerebral activity.

REFERENCES

1. Karbe H, Kertesz A, Davis J, et al. Quantification of functional deficit in Alzheimer's disease using a computer-assisted mapping program for 99mTc-HMPAO SPECT. Neuroradiology. 1994;36:1–6.
2. Mielke R, Pietrzyk U, Jacobs A, et al. HMPAO SPET and FDG PET in Alzheimer's disease and vascular dementia: comparison of perfusion and metabolic pattern. Eur J Nucl Med. 1994;21:1052–1060.
3. Deutsch G, Mountz JM, Katholi CR, Liu HG, Harrell LE. Regional stability of cerebral blood flow measured by repeated technetium-99m-HMPAO SPECT: implications for the study of state-dependent change. J Nucl Med. 1997;38:6–13.
4. Claus JJ, van Harskamp F, Breteler MMB, et al. Assessment of cerebral perfusion with single-photon emission tomography in normal subjects and in patients with Alzheimer's disease: effects of region of interest selection. Eur J Nucl Med. 1994;21:1044–1051.
5. Evans AC, Beil C, Marrett S, Thompson CJ, Hakim A. Anatomical–functional correlation using an adjustable MRI-based region of interest atlas with positron emission tomography. J Cereb Blood Flow Metab. 1998;8:513–530.
6. Holman BL, Zimmerman RE, Johnson KA, et al. Computer-assisted superimposition of magnetic resonance and high-resolution technetium-99m-HMPAO and thallium-201 SPECT images of the brain. J Nucl Med. 1991;32:1478–1484.
7. Sugiura M, Kawashima R, Sadato N, et al. Anatomic validation of spatial normalization methods for PET. J Nucl Med. 1999;40:317–322.
8. Stodilka RZ, Kemp BJ, Msaki P, Prato FS, Nicholson RL. The relative contributions of scatter and attenuation corrections toward improved brain SPECT quantification. Phys Med Biol. 1998;43:2991–3008.
9. Iida H, Narita Y, Kado H, et al. Effects of scatter and attenuation correction on quantitative assessment of regional cerebral blood flow with SPECT. J Nucl Med. 1998;39:181–189.
10. Floyd CE, Jaszczak RJ, Greer KL, Coleman RE. Deconvolution of Compton scatter in SPECT. J Nucl Med. 1985;26:406–408.
11. Lange K, Carson R. EM reconstruction algorithms for emission and transmission tomography. J Comput Assist Tomogr. 1984;8:306–316.
12. Bailey DL, Hutton BF, Walker PJ. Improved SPECT using simultaneous emission and transmission tomography. J Nucl Med. 1987;28:844–851.
13. Kemp BJ, Prato FS, Nicholson RL, Reese L. Transmission computed tomography imaging of the head with a SPECT system and a collimated line source. J Nucl Med. 1995;36:328–335.
14. Xu EZ, Mullani NA, Gould KL, Anderson WL. A segmented attenuation correction for PET. J Nucl Med. 1991;32:161–165.
15. Tan P, Bailey DL, Meikle SR, et al. A scanning line source for simultaneous emission and transmission measurements in SPECT. J Nucl Med. 1993;34:1752–1760.
16. Natterer F. Determination of tissue attenuation in emission tomography of optically dense media. Inverse Problems. 1993;9:731–736.
17. Andersson JLR, Vagnhammer BE, Schneider H. Accurate attenuation correction despite movement during PET imaging. J Nucl Med. 1995;36:670–678.
18. Panin VY, Zeng GL, Gullberg GT. Reconstructions of truncated projections using an optimal basis expansion derived from the cross-correlation of a "knowledge set" of a priori cross-sections. IEEE Trans Nucl Sci. 1998;45:2119–2125.
19. Hosoba M, Wani H, Toyama H, Murata H, Tanaka E. Automated body contour detection in SPECT: effects on quantitative studies. J Nucl Med. 1986;27:1184–1191.
20. Van Dyck CH, Lin H, Smith EO, et al. Comparison of technetium-99m-HMPAO and technetium-99m-ECD cerebral SPECT images in Alzheimer's disease. J Nucl Med. 1996;37:1749–1755.
21. Stodilka RZ, Kemp BJ, Prato FS, Nicholson RL. Importance of bone attenuation in brain SPECT quantification. J Nucl Med. 1998;39:190–197.
22. Licho R, Glick SJ, Xia W, et al. Attenuation compensation in 99mTc SPECT brain imaging: a comparison of the use of attenuation maps derived from transmission versus emission data in normal scans. J Nucl Med. 1999;40:456–463.
23. Juni J. Taking brain SPECT seriously: reflections on recent clinical reports in The Journal of Nuclear Medicine. J Nucl Med. 1994;35:1891–1895.
24. Stodilka RZ, Kemp BJ, Msaki P, Prato FS, Nicholson RL. Retrospective scatter and attenuation correction by inferring anatomy from a head atlas [abstract]. IEEE Med Imaging Conference. 1998.
25. Msaki P, Prato FS, Stodilka RZ, et al. The merits of fully automated rCBF determination in eliminating subjective errors in quantitative SPECT [abstract]. J Nucl Med. 1998;39:106P.
26. Zubal IG, Harrell CR, Smith EO, et al. Computerized three-dimensional segmented human anatomy. Med Phys. 1994;21:299–302.
27. Hoh CK, Dahlbom M, Harris G, et al. Automated iterative three-dimensional registration of positron emission tomography images. J Nucl Med. 1993;34:2009–2018.

28. Hudson HM, Larkin RS. Accelerated image reconstruction using ordered subsets of projection data. *IEEE Trans Med Imaging.* 1994;13:601–609.

29. Lassen NA, Anderson AR, Friberg L, Paulson OB. The retention of 99mTc-d,l-HM-PAO in the human brain after intracarotid bolus injection: a kinetic analysis. *J Cereb Blood Flow Metab.* 1988;8:S13–S22.

30. Huang S-C, Hoffman EJ, Phelps ME, Kuhl DE. Quantitation in positron emission computed tomography: 2. effects of inaccurate attenuation correction. *J Comput Assist Tomogr.* 1979;3:804–814.

31. Andersson JLR, Sundin A, Valind S. A method for coregistration of PET and MR brain images. *J Nucl Med.* 1995;36:1307–1315.

32. Talairach J, Tournoux P, Rayport M, eds. *Co-Planar Stereotaxic Atlas of the Human Brain. Three-Dimensional Proportional System: An Approach to Cerebral Imaging.* New York, NY: Thieme; 1988.

33. Tsui BMW, Zhao XD, Cao ZJ, Frey EC. Reconstruction methods for quantitative brain SPECT. *IEEE Trans Nucl Sci.* 1993;40:214–220.

34. Podreka I, Suess E, Goldenberg G, et al. Initial experience with technetium-99m HM-PAO brain SPECT. *J Nucl Med.* 1987;28:1657–1666.

35. Meikle SR, Dahlbom M, Cherry SR. Attenuation correction using count-limited transmission data in positron emission tomography. *J Nucl Med.* 1993;34:143–150.

36. Tung C-H, Gullberg GT. A simulation of emission and transmission noise propagation in cardiac SPECT imaging with nonuniform attenuation correction. *Med Phys.* 1994;21:1565–1576.

37. Tsao J, Stundzia A, Ichise M. Fully automated establishment of stereotaxic image orientation in six degrees of freedom for technetium-99m-ECD brain SPECT. *J Nucl Med.* 1998;39:503–508.

38. Chawluck JB, Alavi A, Dann, et al. Positron emission tomography in aging and dementia: effect of cerebral atrophy. *J Nucl Med.* 1987;28:431–437.

39. Mangin JF, Frouin V, Bloch I, Bendriem B, Lopez-Krahe J. Fast nonsupervised three-dimensional registration of PET and MR images of the brain. *J Cereb Blood Flow Metab.* 1994;14:749–762.

40. Pietrzyk U, Herholz K, Fink G, et al. An interactive technique for three-dimensional image registration: validation for PET, SPECT, MRI and CT brain studies. *J Nucl Med.* 1994;35:2011–2018.